

Computer Simulations of Morphologically Reconstructed CA3 Hippocampal Neurons

M. MIGLIORE, E. P. COOK, D. B. JAFFE, D. A. TURNER, AND D. JOHNSTON

Institute for Interdisciplinary Applications of Physics, National Research Council, 90123 Palermo, Italy; Division of Neuroscience, Baylor College of Medicine, Houston, Texas 77030; Division of Life Sciences, University of Texas at San Antonio, San Antonio, Texas 78249; and Department of Neurosurgery, Duke University Medical Center, Durham, North Carolina 27710

SUMMARY AND CONCLUSIONS

1. We tested several hypotheses with respect to the mechanisms and processes that control the firing characteristics and determine the spatial and temporal dynamics of intracellular Ca^{2+} in CA3 hippocampal neurons. In particular, we were interested to know 1) whether bursting and nonbursting behavior of CA3 neurons could be accounted for in a morphologically realistic model using a number of the known ionic conductances; 2) whether such a model is robust across different cell morphologies; 3) whether some particular nonuniform distribution of Ca^{2+} channels is required for bursting; and 4) whether such a model can reproduce the magnitude and spatial distribution of intracellular Ca^{2+} transients determined from fluorescence imaging studies and can predict reasonable intracellular Ca^{2+} concentration ($[\text{Ca}^{2+}]_i$) distribution for CA3 neurons.

2. For this purpose we have developed a highly detailed model of the distribution and densities of membrane ion channels in hippocampal CA3 bursting and nonbursting pyramidal neurons. This model reproduces both the experimentally observed firing modes and the dynamics of intracellular Ca^{2+} .

3. The kinetics of the membrane ionic conductances are based on available experimental data. This model incorporates a single Na^+ channel, three Ca^{2+} channels (Ca_N , Ca_L , and Ca_T), three Ca^{2+} -independent K^+ channels (K_{DR} , K_A , and K_M), two Ca^{2+} -dependent K^+ channels (K_C and K_{AHP}), and intracellular Ca^{2+} -related processes such as buffering, pumping, and radial diffusion.

4. To test the robustness of the model, we applied it to six different morphologically accurate reconstructions of CA3 hippocampal pyramidal neurons. In every neuron, Ca^{2+} channels, Ca^{2+} -related processes, and Ca^{2+} -dependent K^+ channels were uniformly distributed over the entire cell. Ca^{2+} -independent K^+ channels were placed on the soma and the proximal apical dendrites. For each reconstructed cell we were able to reproduce bursting and nonbursting firing characteristics as well as Ca^{2+} transients and distributions for both somatic and synaptic stimulations.

5. Our simulation results suggest that CA3 pyramidal cell bursting behavior does not require any special distribution of Ca^{2+} -dependent channels and mechanisms. Furthermore, a simple increase in the Ca^{2+} -independent K^+ conductances is sufficient to change the firing mode of our CA3 neurons from bursting to nonbursting.

6. The model also displays $[\text{Ca}^{2+}]_i$ transients and distributions that are consistent with fluorescent imaging data. Peak $[\text{Ca}^{2+}]_i$ distribution for synaptic stimulation of the nonbursting model is broader when compared with somatic stimulation. Somatic stimulation of the bursting model shows a broader distribution in $[\text{Ca}^{2+}]_i$ when compared with the nonbursting model. Synaptic stimulation in both models produces a $[\text{Ca}^{2+}]_i$ distribution that has a peak around the site of stimulation.

7. In conclusion, this model is able to reproduce realistic bursting, spike frequency adaptation, and $[\text{Ca}^{2+}]_i$ dynamics of hippocampal CA3 neurons using several reconstructed morphologies. In almost all cases changes only in the Ca^{2+} -independent K^+ channel densities and distributions on and near the soma were necessary to reproduce the same electrophysiological behavior in different morphologies. Different modes of firing were not dependent on varying Ca^{2+} and Ca^{2+} -dependent K^+ channel distribution, or on geometric constraints of the cell, but on Ca^{2+} -independent K^+ channel densities and distributions on and near the soma. Morphological factors such as cell geometry and dendritic surface-to-volume ratios, however, did influence $[\text{Ca}^{2+}]_i$ transients and distributions.

INTRODUCTION

Under various conditions of depolarizing current pulses, CA3 pyramidal neurons exhibit different firing characteristics (Scharfman 1993; Wong and Prince 1981). In fact, a short somatic pulse of depolarizing current can trigger a burst in some CA3 cells, and, under long somatic current steps, the firing pattern goes from repetitive bursts (low current) to repetitive single action potentials, without accommodation (higher current) (Wong and Prince 1981). Other CA3 neurons do not burst, but show a train of action potentials with spike frequency adaptation (Scharfman 1993). The mechanisms and processes controlling these characteristics, as well as their frequency and duration, may have an important role in modulating neuronal communication. Details of the membrane events that determine firing behavior have been difficult to sort out experimentally. A major limitation has been the virtual inaccessibility of the dendritic trees. Computer simulations can overcome several of these experimental problems by allowing complete observation of the state of the entire modeled neuron. This approach, however, is only useful if all of the most important ionic currents and processes are included in the model while at the same time the resulting computational load is kept within reasonable limits.

There have been previous models of CA3 hippocampal neurons (e.g., Jaffe et al. 1994; Major et al. 1994; Pinsky and Rinzel 1994; Traub et al. 1991) that provided a valuable starting point for the development of our present model. Although each of these past models reproduced many salient features of CA3 neurons, none could reproduce certain ex-

perimental observations that may have important functional consequences. One model (Traub et al. 1991) used simplified intracellular Ca^{2+} concentration ($[\text{Ca}^{2+}]_i$) dynamics and a reduced morphological structure and therefore could not reproduce the experimental transients and measured distributions of $[\text{Ca}^{2+}]_i$. Another model, which was based on a branched dendritic geometry (Jaffe et al. 1994), used a limited set of membrane mechanisms and did not reproduce the typical firing characteristics of CA3 neurons.

One of the most peculiar firing characteristics that distinguishes CA3 from other hippocampal neurons is their bursting activity, although not all CA3 neurons show bursts. Because of their critical position within the hippocampal circuit, a bursting versus nonbursting CA3 neuron could have important biological consequences. Synchronized populations of cell bursts from the CA3 area have been linked to some electrical waveforms that occur under both physiological and pathological conditions; for example the hippocampal sharp waves during behavioral learning (Buzsáki 1986; Buzsáki et al. 1987) and the interictal spikes during epileptiform discharges (Johnston and Brown 1984).

Our aim was to test whether the bursting and nonburst firing characteristics as well as the spatial and temporal $[\text{Ca}^{2+}]_i$ dynamics of CA3 cells could be accurately reproduced by a computational model. We were interested in understanding what differences, in terms of channel densities and distributions, determined the different modes of firing and $[\text{Ca}^{2+}]_i$ transients and distribution over the entire neuron. In particular, we tested whether a specific voltage-gated Ca^{2+} channel (VGCC) distribution, such as a higher Ca^{2+} channel density in the dendrites than in the soma (Traub et al. 1991), is necessary for bursting. In addition, we also examined how differences in these characteristics depend on the morphological properties of our reconstructed cells. We used a complete set of membrane mechanisms based on the known voltage-gated conductances along with realistic morphologies from actual reconstructed neurons. Results from Ca^{2+} and Na^+ imaging experiments helped determine channel distributions.

We found that bursting and nonbursting behavior could be simulated along with the general features of known Ca^{2+} transients using a uniform distribution of VGCCs and Ca^{2+} -dependent K^+ channels over the entire neuron and Na^+ and Ca^{2+} -independent conductances localized on the soma and proximal dendrites. Furthermore, and somewhat surprisingly, only minor changes in the Ca^{2+} -independent K^+ channel densities were needed to reproduce similar firing behavior across a wide range of CA3 neuron morphology.

METHODS

We performed simulations using the program NEURON (version 4.49), developed by Hines (1993), using a time step of 25 μs on a DEC 3000/400 workstation. This time step resulted in no significant differences during initial test simulations when time steps as low as 1 μs were used. Typical run times were 1 h of CPU time for 1 s of simulation.

Morphological and passive properties

Figure 1, A and B, shows camera lucida renderings of neurons used in our simulations and a schematic representation of the distri-

bution of Na^+ and Ca^{2+} -independent K^+ channels that were used for each cell. The morphometric data for these six different CA3 neurons were provided by different laboratories [R. Fricke for the guinea pig neuron F; D. Amaral for rat CA3b neuron A; and D. Turner for guinea pig neurons T32 and T34 (from CA3a) and T38 and T39 (from CA3b)]. Table 1 reports, for each cell, the number of compartments, the passive characteristics, and the input resistance, using either a purely passive morphology (Passive R_N) or the complete set of conductances (Active R_N).

It should be noted that it would have been possible to use one of the published methods (e.g., Claiborne et al. 1992; Rall et al. 1992; Tsai et al. 1994) to reduce a fully reconstructed neuron to a more simplified geometry. There are two major reasons for not doing so: first, in the present work we are interested in modeling reconstructed neurons to make direct comparisons with (or predictions for) experimental data. Even if appropriate firing patterns are obtained with a lumped geometry (as already demonstrated by Traub et al. 1991), questions about the contribution of detailed dendritic structure to those patterns cannot easily be addressed in such models. Secondly, the methods developed for reducing passive electronic structures into simplified lumped compartments no longer apply with the addition of voltage, time, and Ca^{2+} -dependent channels along with Ca^{2+} diffusion to a dendritic tree. For the purposes of this study we therefore chose to use actual reconstructions of neurons rather than lumped or simplified neuronal geometries for our simulations.

Most of the neurons (all except F) were modeled starting from a set of data points including X , Y , Z , and a diameter measurement, and complemented by a list of their topological connections. Internal subroutines of NEURON automatically generated the resulting full dendritic tree as a set of connected compartments. The F neuron, instead, was already available as a set of compartments from previous studies (Jaffe et al. 1994). For all cells the great majority of the resulting compartments were shorter than 0.1 space constant (λ), with very few compartments up to 0.25 λ long. Figure 2 illustrates the surface-to-volume (S/V) ratio as a function of distance from the soma. As can be seen, other than the typical presence of basal and apical dendritic trees, these cells demonstrate a wide variability in their length, total membrane area, input resistance, and geometry.

In this paper the dendritic shafts were used as the target of synaptic input, and thus explicit modeling of spines would not have significantly affected the electrical behavior of our model. Also, as with other previous models of hippocampal pyramidal cells (Jaffe et al. 1994; Traub et al. 1991), no spines were implicitly included, although it could have allowed us to bring the input resistance of our modeled cells arbitrarily close to the experimental values of 120–150 $\text{M}\Omega$.

Channel kinetics

We modeled a single Na^+ channel, three types of VGCCs (Ca_N , Ca_L , and Ca_T), three Ca^{2+} -independent K^+ channels (K_{DR} , K_A , and K_M), and two Ca^{2+} -dependent K^+ channels (K_C and K_{AHP}). As discussed below, the kinetics for the g_{Na} , g_{K_C} , and $g_{\text{K}_{AHP}}$ conductances were adapted from other published models, changing some parameters when necessary.

The general formalism used to model the other conductances that we decided to include ($g_{\text{K}_{DR}}$, g_{K_A} , g_{K_M} , and $g_{\text{Ca}_{N,L,T}}$) derives from the Hodgkin-Huxley equations for a state variable x , corresponding to a gating particle. This gating particle was assumed to pass over a transition between its open and close states. The expressions for the forward and backward rate constants of this transition, α_x and β_x , for the steady-state value, x_∞ , and for the time constant, τ_x , were derived from the Boltzmann equation (Borg-Graham 1991). The resulting expressions for α_x , β_x , x_∞ , and τ_x are

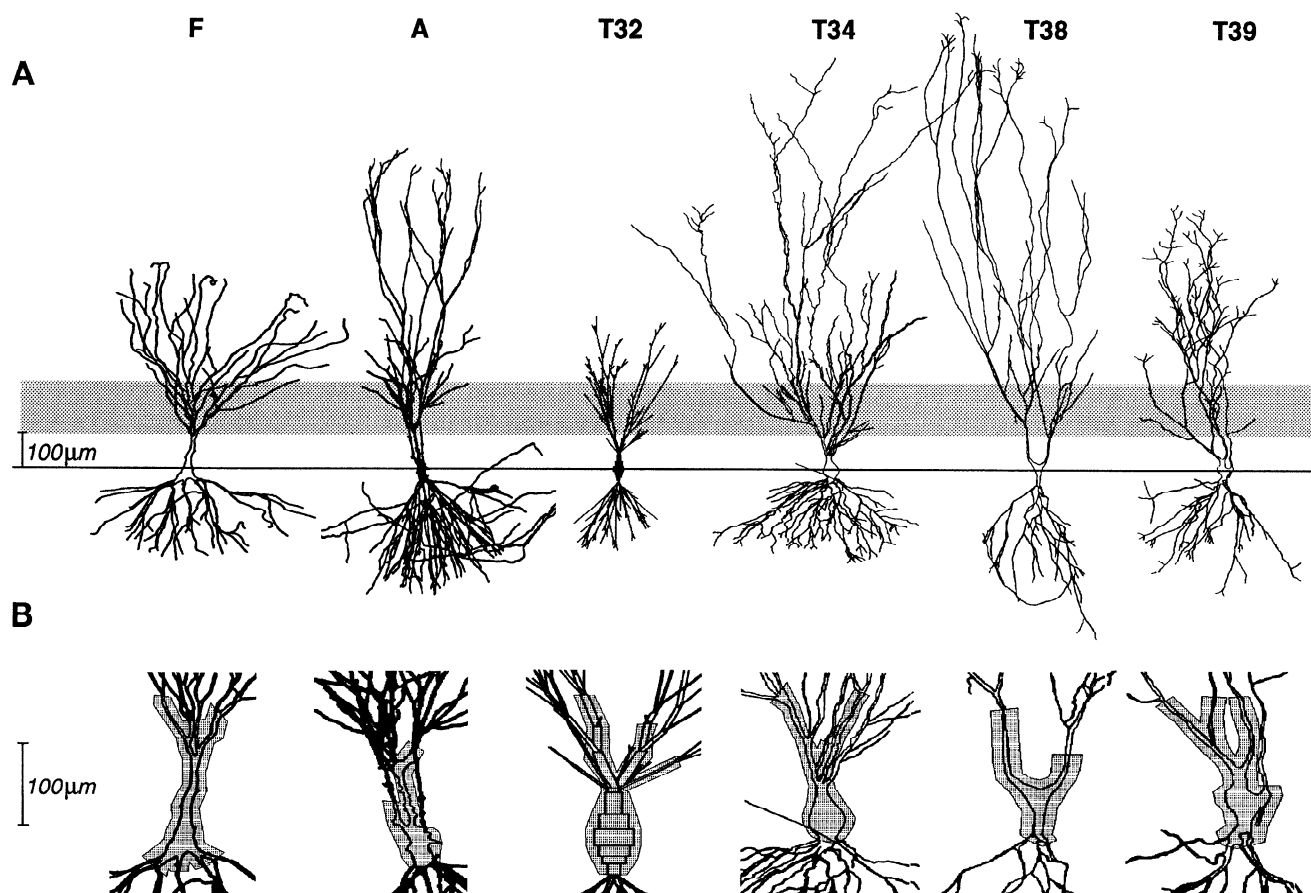


FIG. 1. A: drawings of the reconstructed neurons. The T32 drawing was not available, so its compartmental model is shown instead; the gray shaded areas show the region used for simulations of synaptic stimulation (100–250 μm from soma). B: enlarged region of each neuron showing (shaded area) the somatic and proximal apical dendritic regions where we placed the Na^+ and Ca^{2+} -independent K^+ channels.

$$\alpha_x = \alpha_0 \exp(-\gamma z(V - V_{1/2})F/RT)$$

$$\beta_x = \beta_0 \exp[(1 - \gamma)z(V - V_{1/2})F/RT]$$

$$x_\infty = \alpha_x / (\alpha_x + \beta_x)$$

$$\tau_x = 1 / (\alpha_x + \beta_x)$$

where $\alpha_0 = \beta_0 = \text{constant}$; z , γ , and $V_{1/2}$ are the model parameters for the state variable x ; F is the Faraday's constant; R is the gas constant; and T is the absolute temperature.

The details of the model parameters and channel kinetics are reported in the APPENDIX. We attempted to model channel kinetics as closely as possible to the experimental data from CA3. When these were not available, we used data from CA1 and dentate granule neurons.

g_{Na} . For our sodium conductance we used a previously published model (Traub et al. 1991). It was based on the experimental data for CA1 hippocampal neurons (Sah et al. 1988). We found that by using a higher power for the activation variable m we obtained action potentials with a half-width of ~ 1 ms, as observed experimentally.

g_{KDR} . Different laboratories report different activation and inactivation kinetics for this conductance in hippocampal neurons. For example, $V_{1/2}$ of inactivation is 20 mV more positive in dissociated cultures of rat hippocampal neurons at embryonic day 17–19 (Ficker and Heinemann 1992) than for isolated hippocampal neurons of adult guinea pigs (Numann et al. 1987). The time to peak has been found to be ~ 100 ms (Numann et al. 1987), whereas it was much lower in Ficker and Heinemann (1992). Also, the two

TABLE 1. *Passive properties for each modeled cell*

	F	A	T32	T34	T38	T39
Number of compartments	149	211	287	385	261	262
Membrane area, μm^2	30,108	25,117	10,391	30,319	24,162	14,185
Passive R_N , $\text{M}\Omega$	207	262.8	578.9	202.2	293	446.6
Active R_N , $\text{M}\Omega$	129.6	187	407	150	205.7	311

Input resistances (R_N) have been evaluated with a somatic 1-nA depolarizing current step for passive R_N , and with an 0.2 nA hyperpolarizing current step for active R_N .

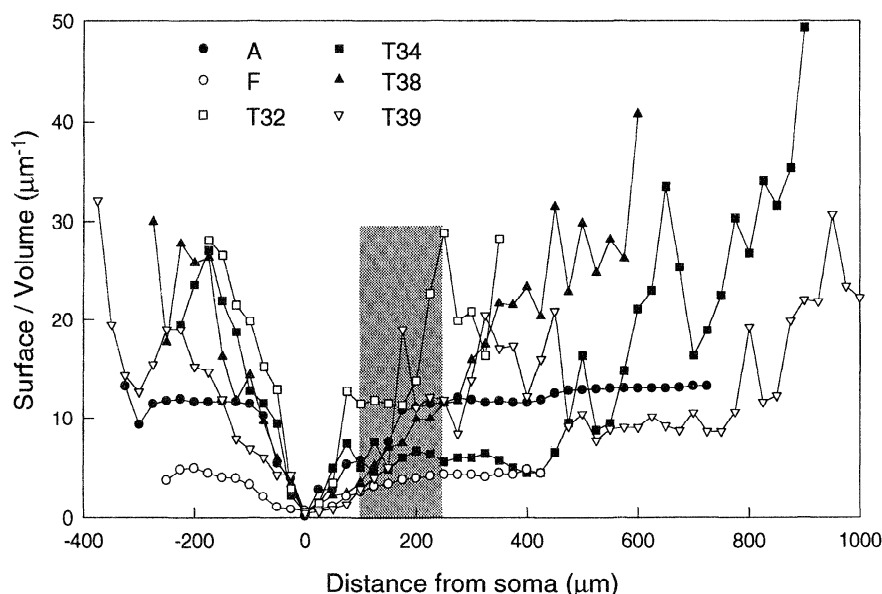


FIG. 2. Surface-to-volume ratio for each cell. Shaded area: region used for synaptic stimulation. Distance is relative to the soma. Negative values are used for basal dendrites.

time constants of inactivation (0.5–3.5 s, Ficker and Heinemann 1992; and 2–3 s, Numann et al. 1987) differ as well. The voltage dependence and the time constants of our activation and inactivation variables are more similar to those found by Ficker and Heinemann. These characteristics, together with the use of a third power for activation, resulted in a current that has a major role in the fast repolarization of the action potential.

g_{K_A} . There is considerable overlap among several different hippocampal cells and preparations for steady-state activation and inactivation curves as well as for the time to peak of this conductance. The time constant of decay, however, has been reported to be 8–10 ms (Ficker and Heinemann 1992) and 20–40 ms (Numann et al. 1987). In our simulations we found that it was easier to simulate a burst when we used a value of 20 ms for this time constant.

g_{K_N} . The activation state variable and time constant for this noninactivating, voltage-dependent K^+ conductance were based on experimental data from bullfrog sympathetic neurons (Adams et al. 1982). Our model is also consistent with experimental data on muscarinic effects in rat hippocampal slice (Williams and Johnston 1990), demonstrating that this noninactivating current is partially open near the resting potential.

$g_{Ca_{NLT}}$. There are at least four types of calcium channels—T, N, L, and P—in hippocampal neurons (Eliot and Johnston 1994; Fisher et al. 1990; Mintz et al. 1992; Mogul and Fox 1991). We used a model that has been previously described (Jaffe et al. 1994). It was based on experimental data for N-, L-, and T-type Ca^{2+} channels in acutely exposed CA3 pyramidal neurons of adult hippocampal neurons (Fisher et al. 1990) and in chick sensory neurons (Fox et al. 1987).

g_{K_C} . This voltage- and Ca^{2+} -dependent K^+ channel was based on a previously published model (Moczydlowski and Latorre 1983) and it is included in the simulation program NEURON. Some adjustments of the two affinity constants, k_1 and k_2 , were found to be necessary to activate this conductance for $[Ca^{2+}]_i$ in the ~100-nM range.

$g_{K_{AHP}}$. We made this Ca^{2+} -activated K^+ conductance with a $([Ca^{2+}]_i)^4$ dependence. Activation and time constant for decay have been adjusted to be roughly consistent with experimental data on hyperpolarizing afterpotentials and repetitive bursts under long depolarizing current pulses.

g_{syn} . For synaptic conductance we used a simple α -function, with $1/\alpha = 3$ ms. Unless otherwise noted, for synaptic stimulations we used a total synaptic conductance of 5 nS, which was distributed among all of the compartments in the region chosen for synaptic activation proportionally to their surface area. A maximum value of $\bar{g}_{syn} = 200$ pS for any one compartment was used and there were no compartments that received a $\bar{g}_{syn} < 30$ pS.

Channel densities and distributions

Exact densities and distributions of channels in hippocampal neurons are not known. Moreover, one would expect some variability both in the density and in the distribution among different cells, even from the same area. Nevertheless, a number of experimental observations were used to establish the initial channel densities and distribution in our model. First, imaging data using sodium-binding benzofuran isophthalate suggest that Na^+ channels, in densities necessary to sustain all-or-none action potentials, are on the soma and the proximal apical dendrites (Jaffe et al. 1992). Second, from fluorescent imaging using fura-2, VGCCs are most likely present over the entire neuron (Jaffe et al. 1992; Regehr and Tank 1992). The densities of Ca^{2+} channels are not known, however, and different Ca^{2+} channel subtypes may be unevenly distributed throughout the entire neuron (Blaxter et al. 1989; Westenbroek et al. 1990, 1992). For simplicity, we distributed VGCCs, Ca^{2+} -dependent K^+ channels (K_C and K_{AHP}), and Ca^{2+} -dependent processes (buffering, pumping, and radial diffusion) uniformly over the entire neuron.

Na^+ and Ca^{2+} -independent K^+ channels were placed only on the soma and on the major apical proximal dendrites up to ~100 μm from the soma, as schematically shown in Fig. 1B. The choice to use only major dendritic trunks, because they would be an extension of the soma, is arbitrary. We found that this assumption, however, led to less variability across different morphologies in the channel densities needed to obtain a burst.

The densities of the channels have been the only parameters that we changed by trial and error to simulate a burst in all of our cells. A few constraints were used to narrow the range of the possible values for some conductances. In fact, for $\bar{g}_{Ca_{NLT}}$ we used the same densities as in a previous work (Jaffe et al. 1994), which had been shown to be consistent with fluorescent imaging data on

CA1. The \bar{g}_{Na} was chosen in such a way to give an action potential of ≥ 70 –80 mV, whereas $\bar{g}_{K_{Dr}}$ was chosen to be high enough to be the major repolarizing conductance after a spike. The $\bar{g}_{K_{AHP}}$ was adjusted to be roughly consistent with the slow afterhyperpolarization (AHP) seen in the experiments after a long depolarizing current pulse.

There were no constraints on the possible values for the densities of the other conductances (i.e. \bar{g}_{K_A} , \bar{g}_{K_M} , and \bar{g}_{K_C}).

Ca²⁺ dynamics

Any model must take into account the Ca²⁺ dynamics inside the cell if experimental data are to be realistically reproduced, especially if Ca²⁺-dependent membrane channels are included. We used a mechanism already included with NEURON that allows Ca²⁺ to radially diffuse inside a compartment. We further included a buffering and a saturable pumping mechanism (see the APPENDIX) to take into account most of those processes that are known to affect [Ca²⁺]_i.

Each compartment was divided into four concentric subshells. This is not strictly necessary, however, to be consistent with optical imaging experiments on Ca²⁺ transients and distributions (Jaffe et al. 1994). In the simulations [Ca²⁺]_i was averaged over all subshells in each compartment to compare the results with Ca²⁺ imaging. Modeling radial Ca²⁺ diffusion allowed the outermost shell to be responsible for the activation of Ca²⁺-dependent K⁺ channels. Further, we believe that using concentric subshells to model [Ca²⁺]_i may have some important consequences in future simulations when other aspects of the role of short-term transients in [Ca²⁺]_i are considered, such as synaptic plasticity.

In some initial test simulations we also included longitudinal [Ca²⁺]_i diffusion. Because it did not affect the outcome of simulations, it was not included in subsequent runs.

RESULTS

Firing modes: bursting

One of the most interesting electrophysiological characteristics of CA3 neurons is their ability to exhibit bursts, which are usually composed of several action potentials riding on a slow depolarizing envelope. These bursts can either be spontaneous or triggered by short pulses of injected current. We are aware of only one other model (Traub et al. 1991) that can reproduce the typical burst and some of its experimental manipulations. That model, however, was developed as a reduced model, which does not include morphometric data or a realistic implementation of [Ca²⁺]_i dynamics. Using such a reduced model it is difficult to reproduce the Na⁺ and Ca²⁺ transients and distributions observed with fluorescent imaging experiments.

Before the appropriate set of conductances needed to obtain a burst could be found, we decided a priori the distribution of channels for each neuron. Ca²⁺-independent K⁺ channels were placed on the soma and on the major proximal apical dendritic trunks, up to ~ 100 μ m from soma, as shown in Fig. 1B. The specific distributions chosen for each cell is arbitrary, i.e., we did not follow a precise rule to place these channels. We found a posteriori, however, that as long as they are restricted roughly to the proximal dendritic region, different distributions have only a very small influence on the ability of a given cell to burst as well as a small influence on the shape of the burst.

We started with the F neuron, using what we thought was a reasonable set of densities for all the conductances. By trial and error we then iteratively adjusted the channel densities, except for \bar{g}_{Ca} , until we obtained a burst in reasonable agreement with experimental data. The same method was then applied to all the other neurons by changing iteratively only the Ca²⁺-independent K⁺ channel densities.

It should be noted that it was not difficult to obtain “a burst” of more than one action potential riding on a depolarizing envelope triggered by a short current pulse. A burst, however, is the result of a small perturbation of an intrinsically unstable equilibrium of the membrane potential, and its exact shape is the result of a very delicate interplay among several ionic currents, in which a paramount role is played by Ca²⁺.

In Fig. 3, typical experimentally recorded CA3 bursts are illustrated with simulated bursts from all our cells under a short somatic or synaptic stimulation. It is interesting to point out that only in the two cells, T32 and T39, which had the highest S/V ratios in the region of synaptic stimulation, were bursts triggered after the first synaptic pulse (Fig. 3C). A second pulse was needed for all the other neurons.

As was the case for the other model of a CA3 neuron (Traub et al. 1991), we have not been able to reproduce in any of our cells the wide spike at the end of a burst. This wide spike is seen in some of the experimental data exclusively during somatic stimulation (e.g., Fig. 3, A1 and A2) and attributed to a large Ca²⁺ influx at the soma. If it is a physiological feature, and not an artifact of the experimental procedures, the reason for this discrepancy might be due to an incomplete repertoire of membrane channels or insufficient characterization of the model membrane conductances. In fact, in the experimental traces (Fig. 3A), the spikes riding on the depolarizing envelope seem to become progressively wider and smaller, suggesting an inactivation of a K⁺ conductance and a possible inactivation of Na⁺ conductance at later spikes.

The set of conductances used to model a burst for each neuron is shown in Fig. 4 (black bars). The conductances required to obtain the same firing characteristics in morphologically very different neurons turned out to be very similar. As indicated above, Ca²⁺ and Ca²⁺-dependent K⁺ channels, not shown in Fig. 4, have been uniformly distributed over the entire neuron and kept the same for all cells and have the following values: $\bar{g}_{CaT} = \bar{g}_{CaD} = 2.5$ mS/cm², $\bar{g}_{CaT} = 0.25$ mS/cm², $\bar{g}_{K_{AHP}} = 0.4$ mS/cm², and $\bar{g}_{K_C} = 0.8$ mS/cm². Only for the A neuron was it necessary to slightly reduce \bar{g}_{K_C} from 0.8 to 0.55 mS/cm² to reproduce the correct shape of the burst.

Figure 5 illustrates a representative example of the time course of the most relevant conductances during a single burst triggered by a short somatic or synaptic stimulation in neuron T39. Although the shape of the burst is quite different in the two cases, there are no qualitative differences in the activation of the individual conductances. The depolarizing envelope results from the time of decay of g_{Ca} being slightly slower than g_{Na} . After the first Na⁺ spike this residual g_{Ca} initiates a self-sustained cascade of events involving a few Na⁺-dependent spikes triggered by a higher and higher Ca²⁺-dependent depolarization. This wave of depolarization

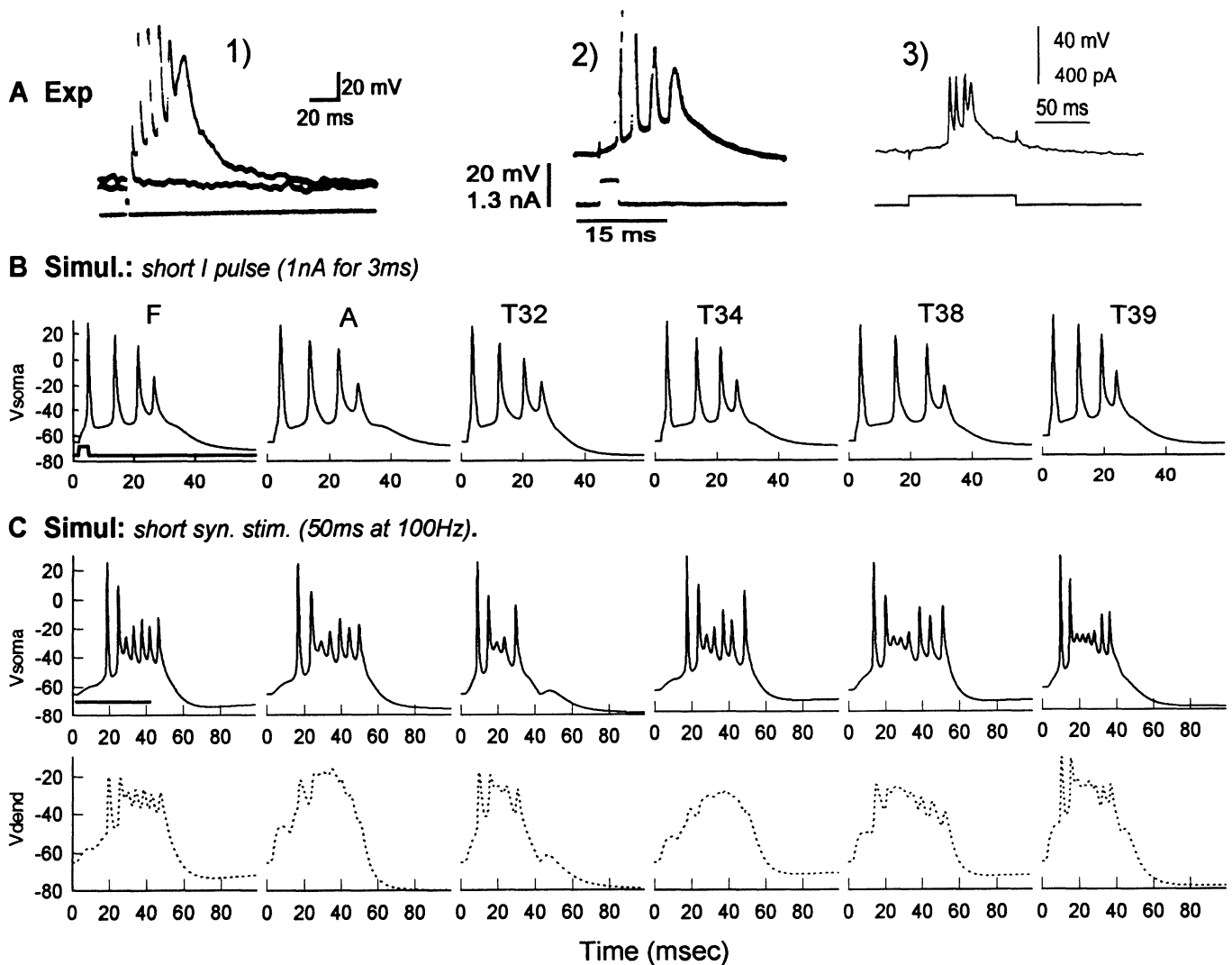


FIG. 3. *A*: examples of experimental bursts. Pictures have been redrawn from 1) Hablitz and Johnston 1981; 2) Wong and Prince 1981; and 3) B. Avery, unpublished observations. *B*: bursts obtained for each cell with a short somatic stimulation (1 nA for 3 ms); *C*: membrane potential of soma (—) and a distal dendrite (· · ·) obtained with a short synaptic stimulation consisting in a train of 5 g_{syn} spaced at 10 ms (50 ms at 100 Hz). Vsoma, membrane potential of soma; Vdend, membrane potential of dendrite.

is ended with the development of a sufficiently high K^+ conductance, especially g_{K_C} and g_{K_M} . $g_{K_{DR}}$ and g_{Ca} reach their maximum value during the first spike, and are smaller and smaller as the burst develops. In contrast, g_{K_C} and g_{K_M} reach their maximum toward the end of the burst. It should be noted that none of the conductances reach their maximum allowable value (\bar{g}) during a burst. In particular, only $\sim 50\%$ of \bar{g} value is reached by g_{Ca} (not shown), $\sim 50\text{--}60\%$ by g_{K_M} , $\sim 10\text{--}20\%$ by $g_{K_{DR}}$ and g_{K_C} , and only $\sim 1\text{--}2\%$ by g_{K_A} and $g_{K_{AHP}}$.

It has been shown experimentally (Hablitz and Johnston 1981; Wong and Prince 1981) and with computer simulations (Traub et al. 1991) that bursts in CA3 can be aborted by an appropriate hyperpolarizing pulse and change their firing mode from repetitive bursts to repetitive action potentials with increasing somatic current injection. These features were reproduced by the model in all of our cells. Examples of increasing somatic current injection in the model and from experimental data are compared in Fig. 6.

Firing modes: nonbursting

Not all CA3 neurons show regular bursting under a depolarizing current step. Some of them show an initial group of three to five spikes firing at higher frequency that become a regular train after the first 200–300 ms (Scharfman 1993). One would probably not expect large differences in the channel densities and distributions between these and normal bursting cells in the same hippocampal area. It should be clear from Fig. 5 that to block the onset of a burst it would be only necessary to increase a K^+ conductance. This would have the effect of blocking the burst after the first spike. The most efficient way to achieve this block is to increase $\bar{g}_{K_{DR}}$ or \bar{g}_{K_A} , both of which have fast activation times. In Fig. 4, we compare the set of conductances we used to simulate a nonbursting (gray bars) and a bursting (black bars) cells. An example of experimental and simulated nonbursting cells is shown in Fig. 7, using neurons A and T34. We found that to have a better agreement with experiments, the most

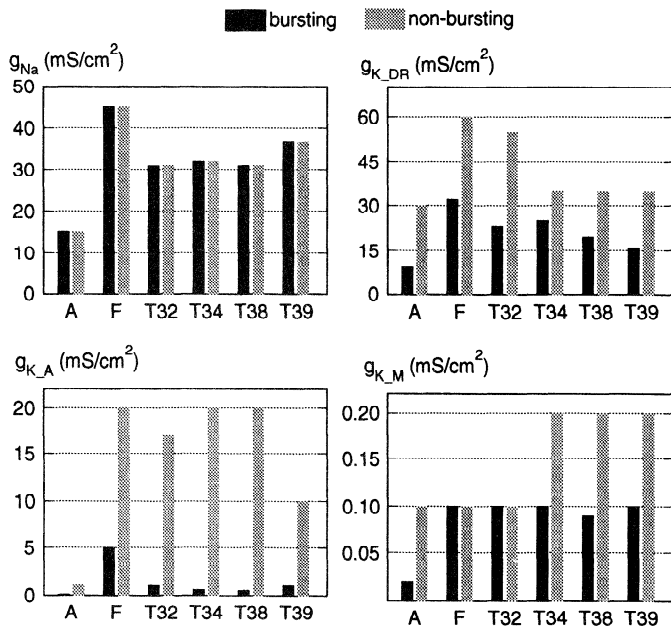


FIG. 4. Peak conductances for each neuron used to simulate bursting and nonbursting behavior.

important difference between a bursting and a nonbursting cell should be in the \bar{g}_{K_A} . A value of \bar{g}_{K_A} that is not sufficiently high or a simple increase of only $\bar{g}_{K_{DR}}$ will yield too many initial spikes. In fact, higher $\bar{g}_{K_{DR}}$ causes a fast and deeper repolarization. As a result, Na^+ and most of the other K^+ conductances will deactivate/inactivate, and the cell will be ready to fire another spike. Even higher values for \bar{g}_{K_A} or \bar{g}_{K_C} would result in single action potentials with long interspike intervals. \bar{g}_{K_M} contributes to the interval between the double spikes.

$[Ca^{2+}]_i$ transients and distributions

The spatial distribution of voltage-gated Ca^{2+} entry can be used as an indicator of relative levels of depolarization throughout the dendritic tree, assuming a relatively homogeneous density of VGCCs in the dendrites. Thus typical experimental $[Ca^{2+}]_i$ transients during long synaptic stimulations are compared with our model in Fig. 8, using the F and T32 cells. The same protocol of stimulation used in the experiments is used and both bursting and nonbursting behavior is examined. As can be seen from Fig. 2, neurons F and T32 have the most different geometries (in terms of the S/V ratio). They can thus be usefully taken as representative of the differences that we found among the cells in the characteristics of the $[Ca^{2+}]_i$ transients and distributions.

Somatic $[Ca^{2+}]_i$ transients (Fig. 8, —) were relatively insensitive to cell morphology, firing modes, or spike frequency. $[Ca^{2+}]_i$ continued to rise at each action potential or burst as long as the stimulation lasted, and there were no significant differences between bursting and nonbursting behavior. The peak value for the soma, in agreement with the experiments of Miyakawa et al. (1992), was rather low, in the 60- to 70-nM range for all cells.

Transients at proximal dendrites (Fig. 8, — — —)

showed two different kinds of behavior, according the S/V ratio in this region. Cells with a higher S/V ratio, such as T32 (see Fig. 2), showed a rapid increase in $[Ca^{2+}]_i$ that reached its maximum value after the first few spikes. Cells with a lower S/V ratio, as in the case of neuron F, showed a more gradual increase of $[Ca^{2+}]_i$, which continued to increase during the entire stimulation phase. Peak values were mostly in the 80- to 110-nM range, and were reached toward the end of the stimulation. Only in T32 did we find a peak value of ~ 220 nM in the proximal dendrites. There were no significant differences between the peak values for bursting or nonbursting behavior, although one or two bursts were generally sufficient to reach the peak value.

For distal dendrites (Fig. 8, - - -), in our case the locus of synaptic stimulation, the local geometric characteristics played a major role. In all cells except F and T34, the peak value for both bursting and nonbursting was reached after the first burst or the first few spikes. This is somewhat different from experiments where, even during a synaptic stimulation, distal dendrites always showed a very low increase in $[Ca^{2+}]_i$ (Miyakawa et al. 1992). It should be noted, how-

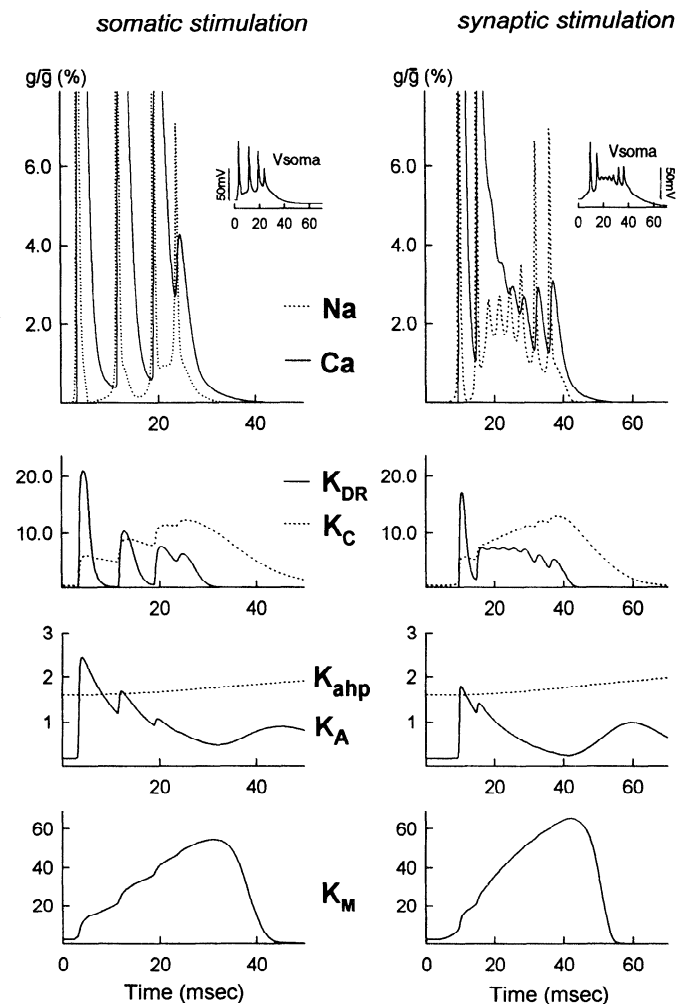


FIG. 5. Example of somatic conductances during a burst obtained with short somatic (left) and synaptic (right) stimulation of the T39 cell. Insets: somatic membrane potential. Protocols of stimulation as in Fig. 3, B and C.

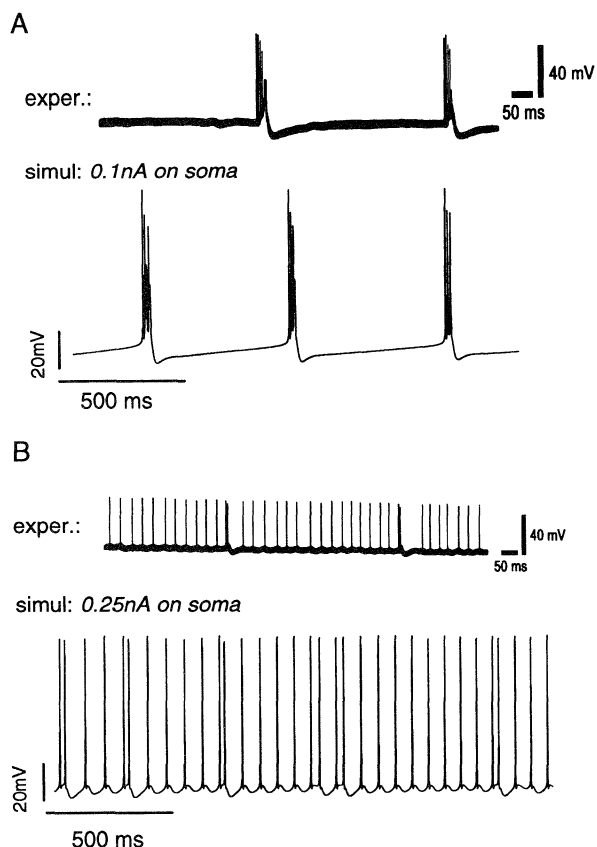


FIG. 6. Example of the different firing modes of a bursting cell under different somatic current injection. Experimental traces are redrawn from Wong and Prince (1981); simulations results are from neuron A. A: 0.1-nA somatic current injection (experimental data are with no current injection). B: 0.25-nA somatic current injection (in the experiments current injection increases with time from 0.2 to 0.5 nA).

ever, that experiments are from CA1 neurons, which typically have a more regular spike frequency adaptation. Furthermore, in these particular imaging experiments, $[Ca^{2+}]_i$ signals from distal dendrites could be underestimated because of the spatial averaging. All cells showed higher peak values for $[Ca^{2+}]_i$ when they were simulated with bursting rather than nonbursting behavior. Because at the site of stimulation, geometry, type of stimulation, and channel densities are exactly the same in the bursting and nonbursting models, this difference can be attributed entirely to the different firing mode (bursts instead of single spikes).

It should be noted that the level of somatic current injection that we have used for these simulations (0.2 nA) produces at least one burst in each cell. For both somatic and synaptic stimulation of bursting cells, the firing properties among the cells may differ between the two extremes shown in Fig. 8, B and C.

Because we were simulating Ca^{2+} influx through VGCCs, we compared our simulations with experiments on calcium imaging in the presence of the *N*-methyl-D-aspartate (NMDA) antagonist 2-amino-5-phosphonovaleric acid. It has been noted that the peak $[Ca^{2+}]_i$ distributions under long somatic or synaptic stimulation of CA1 and CA3 are qualitatively similar, as long as single action potentials are generated (Jaffe et al. 1994). Experiments on CA1 (Miya-

kawa et al. 1992 and Fig. 9B) show that synaptic stimulation of proximal apical dendrites results in higher peak $[Ca^{2+}]_i$ for more distal apical dendrites when compared with somatic current injection. These findings were qualitatively reproduced by our model, as shown in Fig. 9A, where we report the normalized average distribution of peak $[Ca^{2+}]_i$ for bursting and nonbursting firing modes after long somatic and synaptic stimulation (apical dendrites ~ 100 – $250 \mu m$ from soma). It is important to stress that to change the firing characteristics from nonbursting to bursting, we changed only the Ca^{2+} -independent conductances on and near the soma within $\sim 100 \mu m$. Thus, in this model, there were no differences in channel densities and distributions between bursting and nonbursting neurons around the site of synaptic stimulation (100 – $250 \mu m$ from soma). Any difference in the peak $[Ca^{2+}]_i$ distribution for any given neuron is thus caused only by the different firing mode.

For nonbursting cells, somatic stimulation results in a maximum in the region of proximal apical dendrites, in agreement with experiments (Fig. 9). Synaptic stimulation showed essentially the same distribution up to $\sim 100 \mu m$ from soma, with a second maximum for more distal dendrites at around the $200\text{-}\mu m$ region. This latter feature was less prominent when we used a smaller total synaptic conductance (Fig. 9C).

In Fig. 9, peak $[Ca^{2+}]_i$ distribution of somatic stimulation of bursting cells shows the same qualitative features as non-

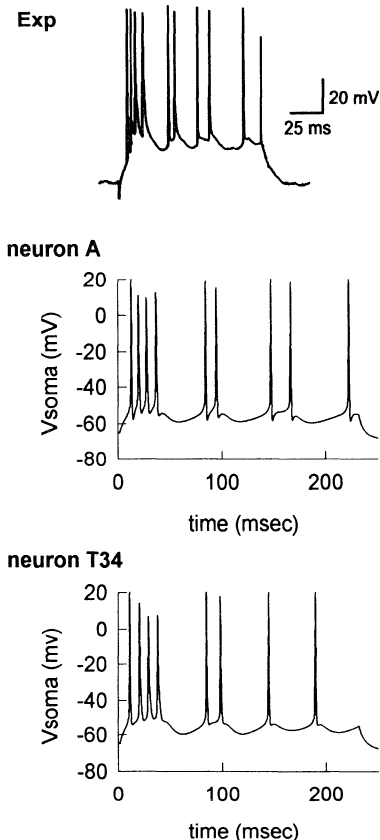


FIG. 7. Example of an experimental trace of a nonbursting CA3 neuron and simulation results for A and T34 for a somatic current step of 0.1 nA. Experimental data are redrawn from Scharfman (1993).

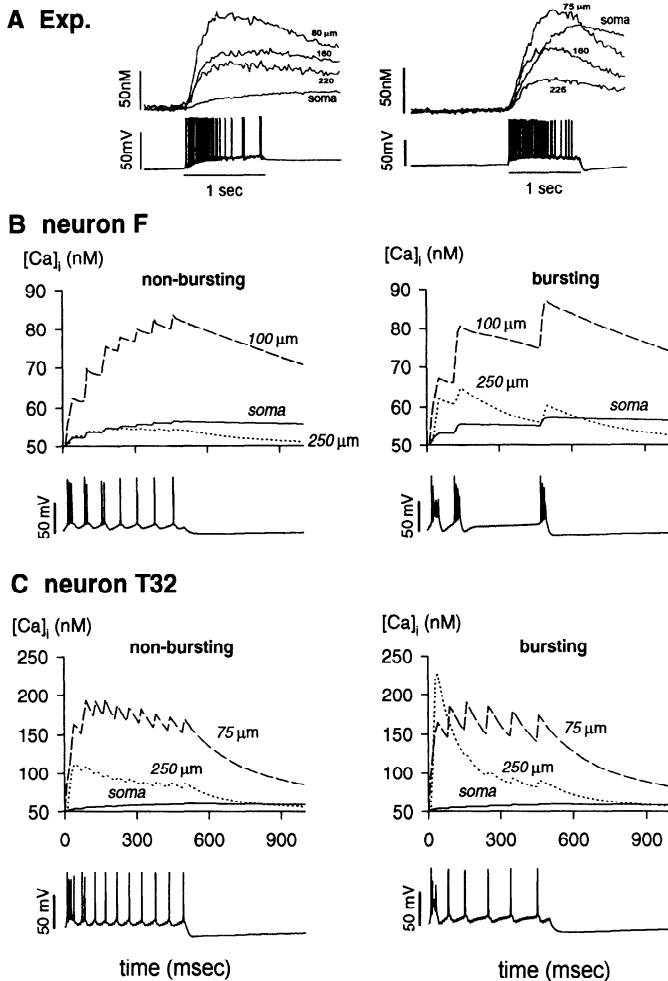


FIG. 8. A: example of experimental data from imaging of CA1 intracellular Ca^{2+} concentration ($[Ca^{2+}]_i$) transients during synaptic stimulation (taken and redrawn from Miyakawa et al. 1992). B and C: examples of simulation results for long synaptic stimulation (500 ms at 100 Hz) from neurons F and T32, respectively. $[Ca^{2+}]_i$ transients at soma (—), proximal dendrites (— — —), and distal dendrites (---).

bursting cells, that is, a maximum value in the region of proximal dendrites. In this case, however, the distribution is significantly broader. Synaptic stimulation of bursting cells, using a total synaptic conductance of 3 or 5 nS, showed that the maximum of the peak $[Ca^{2+}]_i$ distribution was around the most distally stimulated dendrites, ~ 200 – $250 \mu m$ from soma. For synaptic input, $[Ca^{2+}]_i$ is higher than for somatic current injection because bursts elicited from a synaptic stimulation give rise to a longer depolarization (compare Fig. 3, B and C). It should be noted that we are not aware of experimental data on bursting CA3 neurons with which to make better comparisons.

As can be seen in Fig. 9, the variance was generally rather large in the simulation results between neurons. Although this is also true in the experiments, especially for synaptic stimulation, we did not expect such large variability. One possible explanation may be the large variability in the geometric characteristics of the cells. This may cause a large spread of peak $[Ca^{2+}]_i$ distributions when the findings for each cell are averaged. To determine whether this large error

is due to the averaging process or to the intrinsic properties of each cell, we calculated the normalized difference in the peak $[Ca^{2+}]_i$ between synaptic and somatic stimulation ($[Ca^{2+}]_{i-syn} - [Ca^{2+}]_{i-som}$) for each neuron before averaging across the six different cells. This result is reported in Fig. 9D. A value of 0 means no difference between somatic and synaptic stimulation. It is evident that this difference is statistically different from 0, and the results are in qualitative agreement with experiments. This confirms that the reason for the large variance in Fig. 9, A and C, is the large variability among the cells rather than a large variability in the findings for each cell. Near the soma, peak $[Ca^{2+}]_i$ for synaptic stimulation was $\sim 10\%$ lower than for a somatic stimulation. For more distal dendrites a synaptic stimulation resulted in a peak $[Ca^{2+}]_i \approx 10\%$ higher than a somatic stimulation. There were no substantial differences between bursting and nonbursting cells, although for more distal dendrites bursting cells showed a higher difference ($\sim 20\%$).

DISCUSSION

The results showed that it was possible to reproduce bursting, spike frequency adaptation, and $[Ca^{2+}]_i$ dynamics of CA3 hippocampal neurons using the same model on six different reconstructed neurons obtained from different laboratories. This was achieved even though there was a large variability in the morphological parameters among the reconstructed cells used. We do not know to what extent these differences in morphological parameters are physiological (e.g., location of the cell in the CA3 area and age of the animal) or artifacts from the fixation and reconstruction procedures. Using our model, however, we were able to reproduce in all cells the same electrophysiological behavior by changing only the channel densities and distribution of Na^+ and Ca^{2+} -independent K^+ channels on and near the soma, without any change to the state variable kinetics, Ca^{2+} dynamics, Ca^{2+} -dependent K^+ channels (except for $\bar{g}K_c$ in neuron A), or VGCC.

Some studies in other pyramidal cells (e.g., Kim and Connors 1993) seem to suggest a correlation between complex firing properties and cell morphology. In our model, the conditions for eliciting a burst in a neuron are those determined by an appropriate set of conductances at a suitable resting potential, and morphological constraints do not seem to play an overriding role. Because of the interplay among the various conductances the membrane potential becomes unstable near the resting potential, and a small external stimulation can easily elicit a burst. Our model suggests that these conditions are not very different from those in a nonbursting neuron (Fig. 4), because it is sufficient to increase the Ca^{2+} -independent K^+ channel density for a cell to switch from a bursting to a nonbursting behavior. Thus the model predicts that any pharmacological manipulation or a neuromodulator that brings a regular spiking cell close to these conditions (e.g., raising the extracellular K^+ concentration, see Jensen et al. 1994, or adding the K^+ channel blocker TEA to the bath, see Schwartzkroin and Prince 1980) will most likely transform a cell to a burster and vice versa.

In previous simulations (Traub 1982; Traub et al. 1991) it was suggested that "hot spots" or \bar{g}_{Ca} higher in the den-

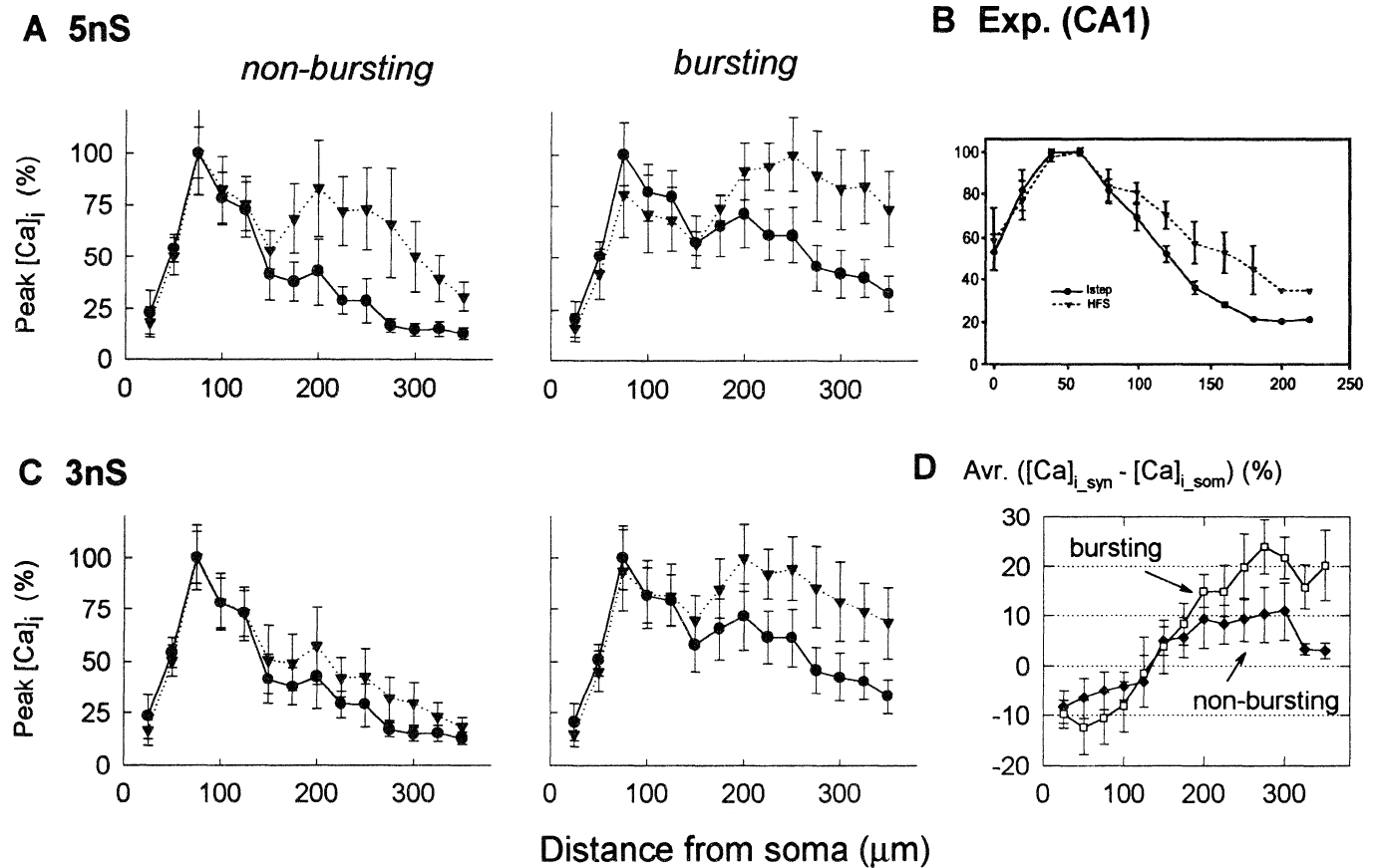


FIG. 9. *A*: normalized peak $[Ca^{2+}]_i$ distribution averaged over all cells simulated as bursting and nonbursting neurons. Circles: long somatic stimulation (0.2 nA for 500 ms). Triangles: long synaptic stimulation (500 ms at 100 Hz), using a total synaptic conductance of 5 nS distributed among all compartments 100–250 μm from soma. *B*: example of experimental data on peak $[Ca^{2+}]_i$ distribution in CA1 neurons (redrawn from Miyakawa et al. 1992). *C*: as in *A*, but using a total synaptic conductance of 3 nS. *D*: normalized difference between somatic and synaptic stimulations averaged over all neurons for bursting (open symbols) and nonbursting (closed symbols) firing modes.

drites than in the soma would be necessary for a cell to show bursting. This would require, however, some specific (e.g., morphogenetic or activity-dependent) mechanism to explain a nonuniform distribution of channels. Although such specific mechanisms may be physiologically reasonable, the results from our modeling suggest that such an asymmetric distribution of channels is not necessary for bursting behavior.

Ca^{2+} spikes, hot spots, or increased \bar{g}_{Ca} were also not necessary to explain the different firing modes of CA3 neurons (bursting and nonbursting) or to be consistent with experimental data on $[Ca^{2+}]_i$ imaging. Dendritic Ca^{2+} spikes (Wong et al. 1979) could significantly enhance burst development, providing an important source of depolarizing current flow. It should be stressed that although Ca^{2+} spikes are easily obtained with our model (by either increasing the total synaptic conductance, including more distal synaptic stimulation, increasing the \bar{g}_{syn} on thinner compartments, or reducing dendritic K^+ conductance), we preferred a more conservative approach, because there is not yet experimental evidence from imaging on the development of dendritic Ca^{2+} spikes.

Although some methods for automatic search through the parameters space have been recently published (Bhalla and

Bower 1993; Foster et al. 1993), we did not explore all the possible sets of conductances that could result in a burst on a given cell. The rationale for that is that the phase space for our model, as for any realistic model, is immense. This means that it is very likely that several different sets of physiologically reasonable conductances will give essentially the same qualitative features that we have shown here.

The K^+ conductances, and especially g_{K_C} , played an important role in the shape of the burst and function as a limiting factor for the onset of a dendritic Ca^{2+} spike, especially where a higher S/V ratio makes the cell more sensitive to Ca^{2+} influx. Because in this model \bar{g}_{K_C} was uniformly distributed over the entire neuron, a relatively small change in this conductance has a significant effect on the electrophysiological properties of the neuron. In general, a $\sim 50\%$ decrease makes the model prone to generate dendritic Ca^{2+} spikes, especially under synaptic stimulation of distal dendrites, and a $\sim 30\%$ increase in \bar{g}_{K_C} would be sufficient to distort or abort a burst. The main role of $g_{K_{DR}}$ is to shape the repolarization phase of a spike. An increase in its density causes this conductance to overcome the Ca^{2+} -dependent depolarizing envelope, and each Na^+ spike will undergo a fast and full repolarization. g_{K_A} and g_{K_M} significantly contribute, at different times, to the shape of a burst. In particular,

g_{K_A} has a role after the first spike, and if its value is sufficiently high the burst is aborted. g_{K_M} , because of its slower kinetics, contributes to the ending part of the burst and, together with $g_{K_{AHP}}$, determines the burst frequency during long current injection in CA3 bursting neurons. $g_{K_{AHP}}$ is also mostly responsible for the slow AHP phase after long current injections.

Local cell geometry has an important role in determining the behavior of $[Ca^{2+}]_i$ transients and distributions for synaptic stimulations, and this was particularly evident in distal apical dendrites. The only two cells that did not reach the maximum value of $[Ca^{2+}]_i$ after the first burst or the first few spikes were neurons F and T34, which both have the lower S/V ratio in this region (see Fig. 2). At the soma, where the S/V ratio is approximately the same for all cells, the time course of $[Ca^{2+}]_i$ consistently showed the same features among the different cells. The same synaptic input on the same local geometry, however, can give qualitatively different $[Ca^{2+}]_i$ dynamics, depending on the firing mode, as evidenced by the qualitatively different distributions among bursting and nonbursting cells in Fig. 9.

Finally, one of the aims of the present paper was also to test whether a realistic model can reproduce the known dynamics of $[Ca^{2+}]_i$ of nonbursting cells and can predict $[Ca^{2+}]_i$ transients and distribution especially for bursting neurons. The latter is especially important because the Ca^{2+} -sensitive dyes used to obtain the fluorescent images of Ca^{2+} influx interfere with the physiological buffering of $[Ca^{2+}]_i$, and this could easily prevent bursting in these experiments. Our model suggests that in a bursting cell the peak $[Ca^{2+}]_i$ distribution can show a localization of Ca^{2+} influx around the site of stimulation, although much lower than what might result from activation, for example, of NMDA receptors on the spines.

APPENDIX

Model Parameters

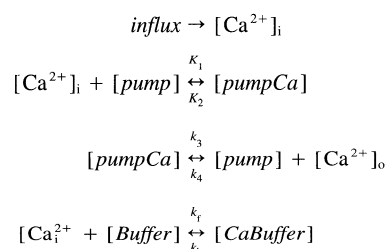
$$R_i = 200 \Omega \cdot \text{cm} \quad \text{resting potential} = -65 \text{ mV} \quad [Ca^{2+}]_o = 2 \text{ mM}$$

$$R_m = 60,000 \Omega \cdot \text{cm}^2 \quad V_K = -91 \text{ mV} \quad \text{resting } [Ca^{2+}]_i = 50 \text{ nM}$$

$$C_m = 1 \mu\text{F}/\text{cm}^2 \quad V_{Na} = 50 \text{ mV}$$

$$Ca^{2+} \text{ diffusion coefficient} = 0.6 \mu\text{m}^2/\text{ms}$$

Schematic of Ca^{2+} dynamics



with $k_1 = 1 \cdot 10^{10} \mu\text{m}^3/\text{ms}$, $k_2 = 5 \cdot 10^6 \text{ ms}^{-1}$, $k_3 = 1 \cdot 10^{10} \text{ ms}^{-1}$, $k_4 = 5 \cdot 10^6 \mu\text{m}^3/\text{ms}$, $[Buffer] + [CaBuffer] = 1.2 \text{ mM}$, and $[pump] + [pumpCa] = 0.2 \text{ mol}/\text{cm}^2$.

Channel kinetics

$$I_{Na} = \bar{g}_{Na} m^3 h (V - V_{Na})$$

[rate constants from Traub et al. (1991)].

$$I_{K_{DR}} = \bar{g}_{K_{DR}} n^3 l (V - V_K)$$

$$\alpha_n = 0.03 \cdot \exp[5 \cdot 0.4(V + 32) \cdot F/RT]$$

$$\beta_n = 0.03 \cdot \exp[5 \cdot 0.6(V + 32) \cdot F/RT]$$

$$\alpha_l = 0.001 \cdot \exp[-2 \cdot (V + 61) \cdot F/RT]$$

$$\beta_l = 0.001$$

$$I_{K_A} = \bar{g}_{K_A} n l (V - V_K)$$

$$\alpha_n = 0.02 \cdot \exp[3 \cdot 0.6(V + 33.6) \cdot F/RT]$$

$$\beta_n = 0.02 \cdot \exp[-1.2 \cdot (V + 33.6) \cdot F/RT]$$

$$\alpha_l = 0.08 \cdot \exp[4(V + 83) \cdot F/RT]$$

$$\beta_l = 0.08$$

$$I_{K_M} = \bar{g}_{K_M} m (V - V_K)$$

$$\alpha_m = 0.006 \cdot \exp[10 \cdot 0.06(V + 55) \cdot F/RT]$$

$$\beta_m = 0.06 \cdot \exp[-9.4(V + 55) \cdot F/RT]$$

$$I_{K_C} = \bar{g}_{K_C} o (V - V_K)$$

(rate const. from Moczydlowski and Latorre (1983), with

$$k_1 = 0.48 \cdot 10^{-3} \text{ mM} \quad \text{and} \quad k_2 = 0.13 \cdot 10^{-6} \text{ mM}).$$

$$I_{K_{AHP}} = \bar{g}_{K_{AHP}} w (V - V_K)$$

$$\alpha_w = 1.3 \cdot 10^{13} \cdot [Ca^{2+}]_i^4 \quad \beta_w = 0.005$$

I_{Ca} : kinetics and rate constants from Jaffe et al. (1994).

$$I_{syn} = \bar{g}_{syn} \cdot (t/\tau) \cdot \exp[-(t - \tau)/\tau] (V - V_{syn})$$

with $\bar{g}_{syn} = 30 \div 150 \text{ pS}$, $\tau = 3 \text{ ms}$, and $V_{syn} = 0$.

M. Migliore thanks M. Hines for considerable help in using NEURON, R. Fricke for the camera lucida drawing of the F neuron, D. Amaral for the NEURON file of the A neuron, and S. Pappalardo and M. Haque for technical assistance.

This work was supported by the Consiglio Nazionale delle Ricerche-PF "Sistemi Informatici e Calcolo Parallelo," National Institute of Mental Health Grants MH-44754, MH-48432, and MH-10475, and the Keck Center for Computational Biology.

Address for reprint requests: M. Migliore, CNR-IAIF, via Archirafi 36, 90123 Palermo, Italy.

Received 27 May 1994; accepted in final form 3 November 1994.

REFERENCES

- ADAMS, P. R., BROWN, D. A., AND CONSTANTIN, A. M-currents and other potassium currents in bullfrog sympathetic neurones. *J. Physiol. Lond.* 330: 537–572, 1982.
- BHALLA, U. S. AND BOWER, J. M. Exploring parameter space in detailed single neuron models: simulations of the mitral and granule cells of the olfactory bulb. *J. Neurophysiol.* 69: 1948–1965, 1993.
- BLAXTER, T. J., CARLEN, P. L., AND NIESEN, C. Pharmacological and anatomical separation of calcium currents in rat dentate granule neurones in vitro. *J. Physiol. Lond.* 412: 93–112, 1989.
- BORG-GRAHAM, L. J. Modelling the non-linear conductances of excitable membranes. In: *Cellular Neurobiology: A Practical Approach*, edited by J. Chad and H. Wheal. New York: IRL, 1991, p. 247–275.
- BUZSAKI, G. Hippocampal sharp waves: their origin and significance. *Brain Res.* 398: 242–252, 1986.
- BUZSAKI, G., HAAS, H. L., AND ANDERSON, E. G. Long-term potentiation

- induced by physiologically relevant stimulus patterns. *Brain Res.* 435: 331–333, 1987.
- CLAIBORNE, B. J., ZADOR, A. M., MAINEN, Z. F., AND BROWN, T. H. Computational models of hippocampal neurons. In: *Single Neuron Computation*, edited by T. McKenna, J. Davis, and S. F. Zornetzer. San Diego, CA: Academic, 1992, p. 61–80.
- ELIOT, L. S. AND JOHNSTON, D. Multiple components of calcium current in acutely-dissociated dentate gyrus granule neurons. *J. Neurophysiol.* 72: 762–777, 1994.
- FICKER, E. AND HEINEMANN, U. Slow and fast transient potassium currents in cultured rat hippocampal cells. *J. Physiol. Lond.* 445: 431–455, 1992.
- FISHER, R. E., GRAY, R., AND JOHNSTON, D. Properties and distribution of single voltage-gated calcium channels in adult hippocampal neurons. *J. Neurophysiol.* 64: 91–104, 1990.
- FOSTER, W. R., PATON, J. F. R., HOPFIELD, J. J., UNGAR, L. H., AND SCHWABER, J. S. Matching neural models to experiment. In: *Computation and Neural Systems*, edited by F. H. Eeckman and J. M. Bower. Norwell, MA: Kluwer, 1993, p. 21–30.
- FOX, A. P., NOWICKY, M. C., AND TSIEN, R. W. Kinetic and pharmacological properties distinguishing three types of calcium currents in chick sensory neurons. *J. Physiol. Lond.* 394: 149–172, 1987.
- HABLITZ, J. J. AND JOHNSTON, D. Endogenous nature of spontaneous bursting in hippocampal pyramidal neurons. *Cell. Mol. Neurobiol.* 1: 325–334, 1981.
- HINES, M. NEURON—a program for simulation of nerve equations. In: *Neural Systems: Analysis and Modeling*, edited by F. Eeckman. Norwell, MA: Kluwer, 1993, p. 127–136.
- JAFFE, D. B., JOHNSTON, D., LASSER-ROSS, N., LISMAN, J. E., MIYAKAWA, H., AND ROSS, W. N. The spread of Na^+ spikes determines the pattern of dendritic Ca^{2+} entry into hippocampal neurons. *Nature Lond.* 357: 244–246, 1992.
- JAFFE, D. B., ROSS, W. N., LISMAN, J. E., LASSER-ROSS, N., MIYAKAWA, H., AND JOHNSTON, D. A model for dendritic Ca^{2+} accumulation in hippocampal pyramidal neurons based on fluorescence imaging measurements. *J. Neurophysiol.* 71: 1065–1077, 1994.
- JENSEN, M. S., AZOUZ, R., AND YAARI, Y. Variant firing patterns in rat hippocampal cells modulated by extracellular potassium. *J. Neurophysiol.* 71: 831–839, 1994.
- JOHNSTON, D. AND BROWN, T. H. Mechanisms of neuronal burst generation. In: *Electrophysiology of Epilepsy*, edited by P. A. Schwartzkroin and H. V. Wheal. London: Academic, 1984, p. 277–301.
- KIM, H. G. AND CONNORS, B. W. Apical dendrites of the neocortex: correlation between sodium- and calcium-dependent spiking and pyramidal cell morphology. *J. Neurosci.* 13: 5301–5311, 1993.
- MADISON, D. V. AND NICOLL, R. A. Control of the repetitive discharge of rat CA1 pyramidal neurones in vitro. *J. Physiol. Lond.* 354: 319–331, 1984.
- MAJOR, G., LARKMAN, A. U., JONAS, P., SACKMANN, B., AND JACK, J. J. B. Detailed passive cable model of whole-cell recorded CA3 pyramidal neurons in rat hippocampal slices. *J. Neurosci.* 14: 4613–4638, 1994.
- MINTZ, I. M., ADAMS, M. E., AND BEAN, B. P. P-type calcium channels in rat central and peripheral neurons. *Neuron* 9: 85–95, 1992.
- MIYAKAWA, H., ROSS, W. N., JAFFE, D. B., CALLAWAY, J. C., LASSER-ROSS, N., LISMAN, J. E., AND JOHNSTON, D. Synaptically activated increases in Ca^{2+} concentration in hippocampal CA1 pyramidal cells are primarily due to voltage-gated Ca^{2+} channels. *Neuron* 9: 1163–1173, 1992.
- MOCZYDŁOWSKI, E. AND LATORRE, R. Gating kinetics of Ca^{2+} -activated K^+ channels from rat muscle incorporated into planar lipid bilayers. *J. Gen. Physiol.* 82: 511–542, 1983.
- MOGUL, D. J. AND FOX, A. P. Evidence for multiple types of Ca^{2+} channels in acutely isolated hippocampal CA3 neurons of the guinea-pig. *J. Physiol. Lond.* 433: 259–281, 1991.
- NUMANN, R. E., WADMAN, W. J., AND WONG, R. K. S. Outward currents of single hippocampal cells obtained from the adult guinea pig. *J. Physiol. Lond.* 393: 331–353, 1987.
- PINSKY, P. F. AND RINZEL, J. Intrinsic and network rhythmogenesis in a reduced Traub model for CA3 neurons. *J. Comput. Neurosci.* 1: 35–60, 1994.
- RALL, W., BURKE, R. E., HOLMES, W. R., JACK, J. J. B., REDMAN, S. J., AND SEGEV, I. Matching dendritic neuron models to experimental data. *Physiol. Rev.* 72: 159–186, 1992.
- REGHER, W. G. AND TANK, D. W. Calcium concentration dynamics produced by synaptic activation of CA1 hippocampal pyramidal cells. *J. Neurosci.* 12: 4202–4223, 1992.
- SAH, P., GIBB, A. J., AND GAGE, P. W. The sodium current underlying action potentials in guinea pig hippocampal CA1 neurons. *J. Gen. Physiol.* 91: 373–398, 1988.
- SCHARFMAN, H. E. Spiny neurons of area CA3c in rat hippocampus slices have similar electrophysiological characteristics and synaptic responses despite morphological variation. *Hippocampus* 3: 9–28, 1993.
- SCHWARTZKROIN, P. A. AND PRINCE, D. A. Effects of TEA on hippocampal neurons. *Brain Res.* 186: 169–181, 1980.
- STORM, J. F. Potassium currents in hippocampal pyramidal cells. In: *Progress in Brain Research*, edited by J. Storm-Mathisen, J. Zimmer, and O. P. Ottersen. Amsterdam: Elsevier, 1990, vol. 83, p. 161–187.
- TRAUB, R. D. Simulation of intrinsic bursting in CA3 hippocampal neurons. *Neuroscience* 7: 1233–1242, 1982.
- TRAUB, R. D., WONG, R. K. S., MILES, R., AND MICHELSON, H. A model of a CA3 hippocampal pyramidal neuron incorporating voltage-clamp data on intrinsic conductances. *J. Neurophysiol.* 66: 635–650, 1991.
- TSAI, K. Y., CARNEVALE, N. T., CLAIBORNE, B. J., AND BROWN, T. H. Efficient mapping from neuroanatomical to electrotonic space. *Network* 5: 21–46, 1994.
- WESTENBROEK, R. E., AHILJANIAN, M. K., AND CATTERALL, W. A. Clustering of L-type Ca^{2+} channels at the base of major dendrites in hippocampal pyramidal neurons. *Nature Lond.* 347: 281–284, 1990.
- WESTENBROEK, R. E., HELL, J. W., WARNER, W., DUBEL, S. J., SNUTCH, T. P., AND CATTERALL, W. A. Biochemical properties and subcellular distribution on an N type calcium channel $\alpha 1$ subunit. *Neuron* 9: 1099–1115, 1992.
- WILLIAMS, S. AND JOHNSTON, D. Muscarinic depression of synaptic transmission at the hippocampal mossy fiber synapse. *J. Neurophysiol.* 64: 1089–1097, 1990.
- WONG, R. K. S. AND PRINCE, D. A. Afterpotential generation in hippocampal pyramidal cells. *J. Neurophysiol.* 45: 86–97, 1981.
- WONG, R. K. S., PRINCE, D. A., AND BASBAUM, A. I. Intradendritic recordings from hippocampal neurons. *Proc. Natl. Acad. Sci. USA* 76: 986–990, 1979.